JOURNAL OF SPACECRAFT AND ROCKETS
Vol. 39, No. 6, November–December 2002

Power-Law Shaped Leading Edges in Rarefied Hypersonic Flow

Wilson F. N. Santos*
National Institute for Space Research, 12630-000 Cachoeira Paulista, Brazil
and
Mark J. Lewis†
University of Maryland, College Park, Maryland 20742

A numerical study is reported on power-law shaped leading edges situated in a rarefied hypersonic flow. The work is motivated by interest in investigating the flowfield properties of power-law shaped leading edges as possible candidates for blunting the geometry of hypersonic leading edges. The sensitivity of both the flowfield structure and surface quantities to shape variations of such leading edges is calculated by using a direct simulation Monte Carlo method. Particular attention is focused on the pressure gradient along the body surface and on the heat transfer to the body. Calculations showed that the pressure coefficient for the flow conditions considered is in surprising agreement with that obtained by simple Newtonian theory, which predicts that a class of power-law shapes exhibits aerodynamic behavior different from that expected for classical blunt shape. Simulations also showed that the stagnation point heating on power-law leading edges with a finite radius of curvature follows the same relation as that for classical blunt body. However, for those leading edges with zero radii of curvature, the heat transfer behavior follows another pattern in the vicinity of the stagnation point, reaching a finite value exactly at the nose.

Nomenclature

a = constant in power-law body equation
c_d = total drag coefficient, $2F/\rho_\infty U_\infty^2 H$
c_f = skin-friction coefficient, $2\tau_w/\rho_\infty U_\infty^2$
c_h = heat transfer coefficient, $2q_w/\rho_\infty U_\infty^3$
c_p = pressure coefficient, $2(p_w - p_\infty)/\rho_\infty U_\infty^2$
F = total drag force, N
H = body height at the base, m
Kn_∞ = freestream Knudsen number
L = body length, m
M_∞ = freestream Mach number
n = body power-law exponent, number density
p_∞ = freestream pressure, N/m^2
q = heat flux, W/m^2
R = circular cylinder radius, m; gas constant, J/kmol · K
R_c = radius of curvature, m
Re_∞ = freestream Reynolds number
S_∞ = freestream molecular speed ratio
s = arc length, m
T_w = wall temperature, K
T_∞ = freestream temperature, K
U_∞ = freestream velocity, m/s
u_w = velocity slip, m/s
v = normal velocity, m/s
x, y = Cartesian axis in physical space
Δt = time step, s
η = coordinate normal to body surface
θ = wedge half-angle, body slope angle, deg
λ_∞ = freestream mean free path, m
μ_∞ = freestream viscosity, Ns/m^2
ρ_∞ = freestream density, kg/m^3
τ = body slenderness parameter, H/L
τ_w = shear stress, N/m^2

Introduction

FOR flight at hypersonic speeds, the vehicle leading edges must be sufficiently blunt to reduce the heat transfer rate to acceptable levels and possibly to allow for internal heat conduction. The use of blunt-nosed shapes tends to alleviate the aerodynamic heating problem because the heat flux for blunt bodies scales inversely with the square root of the nose radius. In addition, the reduction in heating rate for a blunt body is accompanied by an increase in heat capacity, due to the increased volume. Because the stagnation region is generally the most thermally stressed zone, this particular region is of considerable practical, as well as theoretical, interest. Designing a hypersonic vehicle leading edge involves a tradeoff between making the leading edge sharp enough to obtain acceptable aerodynamic and propulsion efficiency and blunt enough to reduce the aerodynamic heating in the stagnation region.

The study of a hypersonic blunt-body flowfield has been of interest for several decades. Numerous studies[1−13] have been done with the power-law form, $y \sim x^n$, $0 < n < 1$, representing blunt geometries. The major interest had focused on finding solutions to the hypersonic small disturbance form of the inviscid adiabatic-flow equations.

The equations of motion for hypersonic flow over slender bodies can be reduced to a simpler form by incorporating the hypersonic slender-body approximations.[14] The reduced equations are valid provided that $\tau^2 \ll 1$ and $(M_\infty \tau)^{-2}$ is not near one, where M_∞ is the freestream Mach number and τ is a slenderness parameter. By using the hypersonic slender-body approximations, Yasuhara[1] obtained a similar solution of the hypersonic viscous flow past an axisymmetric power-law body for a special case of $n = \frac{3}{4}$. This work investigated the slenderness effect of the body in the region of strong interaction between the boundary layer on the body surface and the shock wave, which was assumed to be attached to the nose of the body. The solution is not correct near the nose where the hypersonic slender-body approximation $\tau^2 \ll 1$ is violated.

Lees and Kubota[2] observed that similarity exists for hypersonic flows whenever the shock shape follows a power-law variation with the streamwise distance, provided that the hypersonic slender-body equations are considered in the limit as $(M_\infty \tau)^{-2} \to 0$. According to their work, a detailed study of the equations of motion showed that flow similarity is possible for a class of bodies of the form x^n, provided that $\frac{2}{3} < n < 1$ for a two-dimensional body and $\frac{1}{2} < n < 1$ for an axisymmetric body. The similarity solutions referred to herein are solutions for self-similar flows, that is, flows in which the flowfield between the shock wave and the body can be expressed in terms

---

Received 14 March 2002; revision received 25 July 2002; accepted for publication 12 August 2002. Copyright © 2002 by the American Institute of Aeronautics and Astronautics, Inc. All rights reserved. Copies of this paper may be made for personal or internal use, on condition that the copier pay the $10.00 per-copy fee to the Copyright Clearance Center, Inc., 222 Rosewood Drive, Danvers, MA 01923; include the code 0022-4650/02 $10.00 in correspondence with the CCC.

*Researcher, Combustion and Propulsion Laboratory; wilson@lcp.inpe.br.

†Professor, Department of Aerospace Engineering; lewis@eng.umd.edu. Associate Fellow AIAA.

of functions that, in suitable coordinates, are independent of one of the coordinate directions.

Mirels[3] discussed at length the application of hypersonic slender-body theory to obtain solutions for power-law bodies in a unified way. He also presented an analysis of perturbed power-law body shapes. Freeman et al.[4] and Beavers[5] have studied experimentally the hypersonic flow on axisymmetric power-law bodies. They have presented detailed shock-shape data for a series of power-law bodies and registered some disagreement with other experimental results in the literature. Guiraud et al.[6] have discussed at length the axisymmetric flow around a more extensive class of simple bodies, that is, axisymmetric power-law bodies in the framework of the hypersonic slender-body approximations for an infinite Mach number. Hypersonic flows around axisymmetric power-law slender bodies for finite Mach number and low angle of attack have been studied by Merlen and Andriamanalina.[9] The results are obtained by applying a small perturbation expansion of self-similar solutions using the equivalence principle.

Mason and Lee[10] have conducted a study of minimum-drag body shapes in the supersonic and hypersonic flow regimes. Their numerical results showed that power-law bodies can have low-drag shapes when the exponent n is approximately 0.7. They have suggested the possibility of a difference between shapes geometrically sharp ($\mathrm{d}r/\mathrm{d}x \neq \infty$ at $x = 0$) and shapes that behave aerodynamically as if they were sharp. Mason and Lee[10] showed that theoretically derived supersonic and hypersonic minimum-drag axisymmetric shapes can have an angle of the initial slope ($\mathrm{d}r/\mathrm{d}x \to \infty$) of 90 deg, yet have zero radius of curvature. Therefore, they are geometrically blunt. By performing a Newtonian flow analysis on axisymmetric power-law bodies, Mason and Lee[11] further improved the meaning of aerodynamically, as opposed to geometrically, sharp and blunt shapes. They showed that, for values of $0 < n < \frac{1}{2}$, the leading-edge radius of curvature goes to infinite at the nose, a characteristic of a blunt body. For values of $\frac{1}{2} < n < 1$, the leading-edge radius of curvature approaches zero at the nose, a characteristic of a sharp body. For values of $\frac{2}{3} < n < 1$, the computational investigation predicts that the derivative of the pressure coefficient with respect to the arc length $\mathrm{d}c_p/\mathrm{d}s \to -\infty$ at the nose, a characteristic of a sharp body. In this way, there is a class of body shapes given by $\frac{1}{2} < n < \frac{2}{3}$, for which the leading edge may behave aerodynamically like a blunt body, even though the leading-edge radius of curvature is zero, as well as another class given by $\frac{2}{3} < n < 1$, for which the leading edge may behave like aerodynamically sharp bodies.

Merlen et al.[12] have studied waverider configurations derived from hypersonic flows around axisymmetric power-law bodies at low angle of attack. Their solutions were obtained in the framework of the hypersonic small-disturbance theory. Finally, O'Brien and Lewis[13] have investigated power-law shaped leading edges for possible use on hypersonic waverider vehicles. A numerical analysis was performed considering a two-dimensional inviscid flow. Results were compared to a corresponding circular cylinder to determine which geometry would be better suited as a blunting profile. Their analysis showed that circular cylinders provide smaller shock standoff and drag for equivalent stagnation point heating under the range of conditions investigated.

The purpose of this paper is to investigate the effect of the power-law exponent on the flowfield structure and on the surface quantities over such leading edges. The flow conditions represent those experienced by a spacecraft at altitude of 70 km. This altitude is associated with the transitional regime that is characterized by the Knudsen number Kn of the order of 10^{-2} or larger. In such a circumstance, the degree of molecular nonequilibrium is such that the Navier–Stokes equations are inappropriate. In the current study, a direct simulation Monte Carlo (DSMC) method is used to calculate the rarefied hypersonic two-dimensional flow. Attention will be addressed to the analysis of the pressure gradient along the surface and the stagnation point heating.

Table 1 Characteristics dimensions of the power-law shapes

n	a, m^{1-n}	L, m	τ
$\frac{1}{2}$	4.16711×10^{-2}	1.39628×10^{-2}	0.705
0.6	5.72571×10^{-2}	1.67554×10^{-2}	0.588
$\frac{2}{3}$	7.00993×10^{-2}	1.86171×10^{-2}	0.529
0.7	7.73661×10^{-2}	1.95479×10^{-2}	0.504
$\frac{3}{4}$	8.94383×10^{-2}	2.09442×10^{-2}	0.470
0.8	1.03049×10^{-1}	2.23404×10^{-2}	0.441

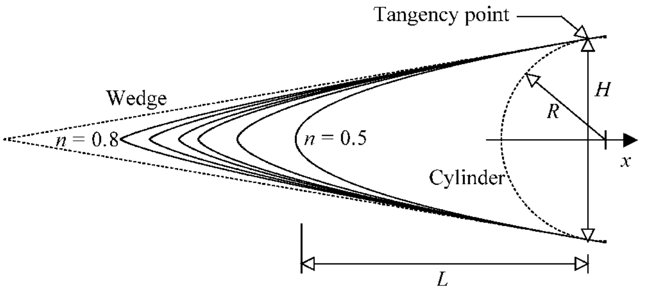

Fig. 1 Leading-edge geometry.

Leading-Edge Geometry Definition

In dimensional form, the body power-law shapes are given by the following expression:

$$y = ax^n \tag{1}$$

where a is the power law constant that is a function of n.

The power-law shapes are modeled by assuming a sharp leading edge of half-angle θ with a circular cylinder of radius R inscribed tangent to this wedge. The power law shapes, inscribed between the wedge and the cylinder, are also tangent to the wedge and the cylinder at the same common point, where they have the same slope angle. It is assumed a wedge half-angle of 10 deg, a circular cylinder diameter of 10^{-2}m, and power-law exponents of $\frac{1}{2}$, 0.6, $\frac{2}{3}$, 0.7, $\frac{3}{4}$, and 0.8. Figure 1 illustrates this construction schematically for the range to be investigated in this work.

From geometric considerations, the power-law constant a, the body height H and the body length L are obtained by matching slope on the wedge, circular cylinder, and power-law body at the tangency point. The common body height H at the tangency point is equal to $2R\cos\theta$. In this way, for the six power-law exponents to be investigated in this work, the power-law constant a, the body length L, and the body slenderness parameter τ are listed in Table 1.

Computational Method and Procedure

The DSMC method is now a well-established technique. It has been recognized as an extremely powerful technique capable of predicting an almost unlimited variety of rarefied flowfields in the regimes where neither the Navier–Stokes nor the free-molecular approaches are appropriate. The DSMC algorithm used in the current study is built around the same basic physical concepts as described by Bird.[15] In this study, the molecular collisions are modeled using the variable hard sphere (VHS) molecular model[16] that treats molecules as hard spheres as far as the scattering angle distribution is concerned, but in which the collision cross section depends on the relative speed of colliding molecules. The energy exchange between kinetic and internal modes is controlled by the Borgnakke–Larsen statistical model.[17] The simulations are for low-energy flow conditions where there are no chemical reactions. Therefore, simulations are performed using a nonreactive air as working fluid, with two chemical species, N_2 and O_2.

The probability of an inelastic collision determines the rate at which energy is transferred between the translational and internal modes after an inelastic collision. For a given collision, the probabilities are designated by the inverse of the relaxation numbers, which correspond to the number of collisions necessary, on average, for a molecule to relax. The relaxation numbers are assumed to be constant, on the order of 5 for rotation and 50 for vibration. The vibrational temperature is controlled by the distribution of energy between the translational and rotational modes after an inelastic collision. The mechanics of vibrational energy exchange are also computed by the Borgnakke–Larsen[17] approach with the postcollision vibrational energy levels sampled from the discrete form of the simple harmonic oscillator.[15] The freestream coefficient of viscosity μ_∞ and freestream mean free path λ_∞ are evaluated from a consistent definition[18] by using the VHS collision model with the temperature exponents equal to 0.74 and 0.77 for N_2 and O_2, respectively. Diffuse reflection with full thermal accommodation is assumed for the gas–surface interaction.

The computational domain used for the calculations is large enough so that body disturbances do not reach the upstream and side boundaries, where freestream conditions are specified. The flowfield is divided into a number of regions, and each one of them has a separate value of time step Δt and scaling factor F_N, which relates the number of real molecules to the number of computational molecules. The ratio of these two quantities is the same in every region. The number of regions differs for each power-law exponent n investigated. The cell dimensions must be such that the change in flow properties across each cell is small; hence, the cell dimension is less than the local mean free path. Each cell is divided into four subcells, the smallest unit of physical space, where the collision partners are selected for the establishment of the collision rate. Also, time is advanced in discrete steps such that each step is small in comparison with the mean collision time. A view of the computational domain is depicted in Fig. 2. Advantage may be taken of the flow symmetry to reduce the computational domain. Therefore, only one-half of the body needs to be considered. The grid generation scheme, the effect of grid resolution, and the complete validation process employed in this study are described in detail in Ref. 19.

Table 2 Freestream conditions and flow parameters

Parameter	Value
Working fluid	$N_2 + O_2$
Altitude	70 km
Temperature T_∞	220.0 K
Pressure p_∞	5.582 N/m^2
Density ρ_∞	8.753×10^{-5} kg/m^3
Viscosity μ_∞	1.455×10^{-5} Ns/m^2
Number density n_∞	1.8209×10^{21} m^{-3}
Velocity U_∞	3.56 km/s
Molecular weight	28.96 kg/kg mole
Molecular mass O_2	5.312×10^{-26} kg
Molecular mass N_2	4.65×10^{-26} kg
Molecular diameter O_2	4.01×10^{-10} m
Molecular diameter N_2	4.11×10^{-10} m
Mole fraction O_2	0.237
Mole fraction N_2	0.763
Degree of freedom O_2	5
Degree of freedom N_2	5
Viscosity index O_2	0.77
Viscosity index N_2	0.74
Mean free path λ_∞	9.03×10^{-4} m
Reynolds number Re_∞	21455 m^{-1}
Mach number M_∞	12
Knudsen number Kn_∞	0.0903
Molecular speed ratio S_∞	9.4

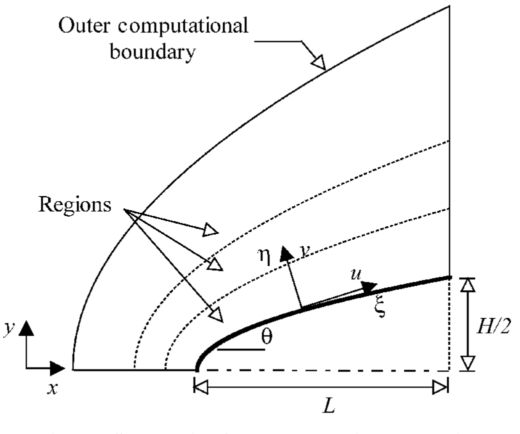

Fig. 2 Schematic of the computational domain.

The freestream and flow conditions used in the present calculations are those given by Bertin[20] and summarized in Table 2. The freestream velocity U_∞ is assumed to be constant at 3.5 km/s, which corresponds to freestream Mach number $M_\infty = 12$. The wall temperature T_w is assumed constant at 880 K, chosen to be four times the freestream temperature. The overall Knudsen number is defined as the ratio of the molecular mean free path in the freestream gas to a characteristic dimension of the flowfield. In the present study, the characteristic dimension was defined as being the diameter of the circular cylinder. Therefore, the freestream Knudsen number corresponds to $Kn_\infty = 0.0903$. Finally, the freestream Reynolds number per unit meter Re_∞ is 2.1455×10^4.

Computational Results and Discussion

Attention is now focused on the flowfield properties and surface quantities calculations obtained from the DSMC results. The simulations were performed, as mentioned earlier, for power-law exponents of $\frac{1}{2}$, 0.6, $\frac{2}{3}$, 0.7, $\frac{3}{4}$, and 0.8. The present calculations correspond to freestream Mach number of 12, wall temperature of 880 K, and freestream conditions associated to an altitude of 70 km (Table 2).

Flowfield Structure

Normal velocity profiles along the stagnation streamline and their dependence on the power-law exponent are illustrated in Fig. 3. The normal velocity profile for the circular cylinder case is also shown in Fig. 3. Each profile has been taken through cell centroids that lie very close to the stagnation line and, therefore, can be considered as being along the stagnation streamline. In this case η/λ_∞ is the dimensionless distance away from the body (Fig. 2). In Fig. 3, the normal velocity v is expressed as a fraction of the freestream velocity U_∞. As can be seen, these profiles show a gradual merging of the shock layer and shock wave with a decrease in the power-law exponent n. As n increases, the velocity profile becomes steeper, indicating that the shock structure becomes thinner. For instance, the velocity reduction at a distance of one freestream mean free path λ_∞ upstream of the leading edge is around 90% for the circular cylinder, 60% for the $n = \frac{1}{2}$ case, and only 10% for the $n = 0.8$ case.

When rarefied flows are simulated, the computational flow domain must extend far enough upstream of the body to provide ample opportunity for freestream molecules to interact with those molecules that have reflected from the body and are diffusing into

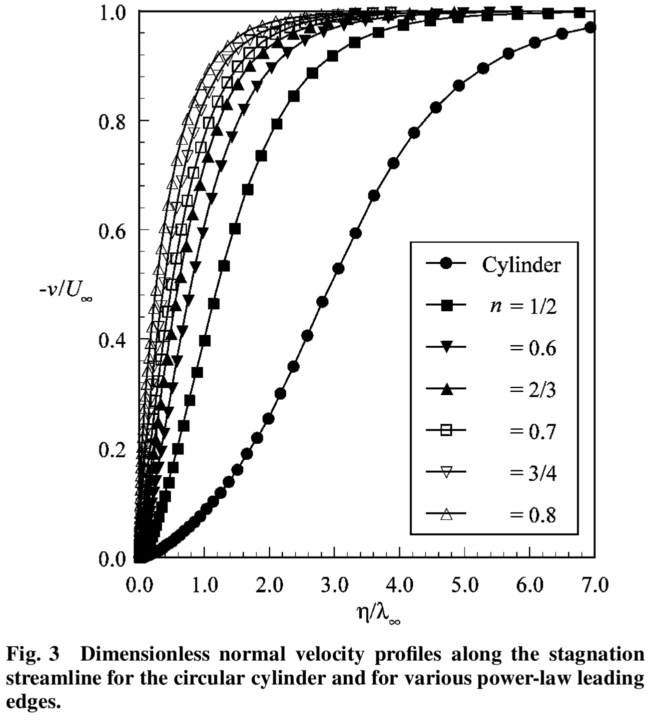

Fig. 3 Dimensionless normal velocity profiles along the stagnation streamline for the circular cylinder and for various power-law leading edges.

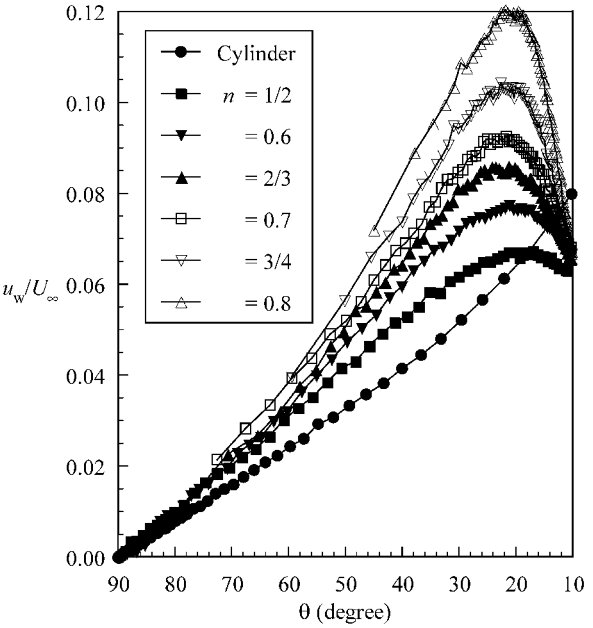

Fig. 4 Dimensionless velocity slip profiles along the body surface for the circular cylinder and for various power-law leading edges.

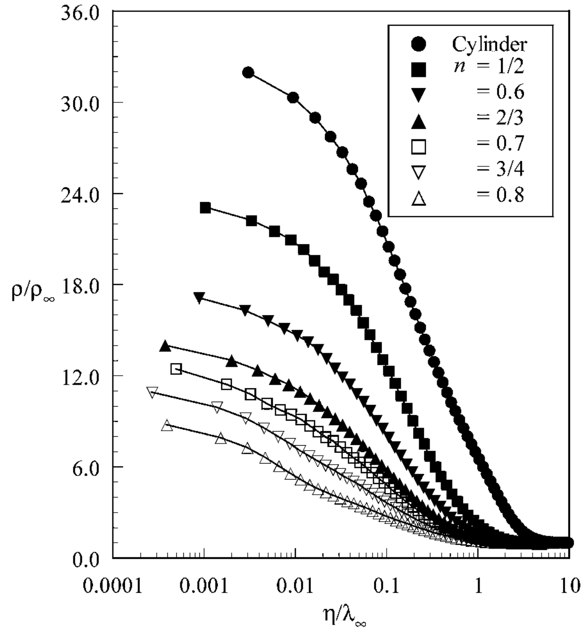

Fig. 5 Dimensionless density profiles along the stagnation streamline for the circular cylinder and for various power-law leading edges.

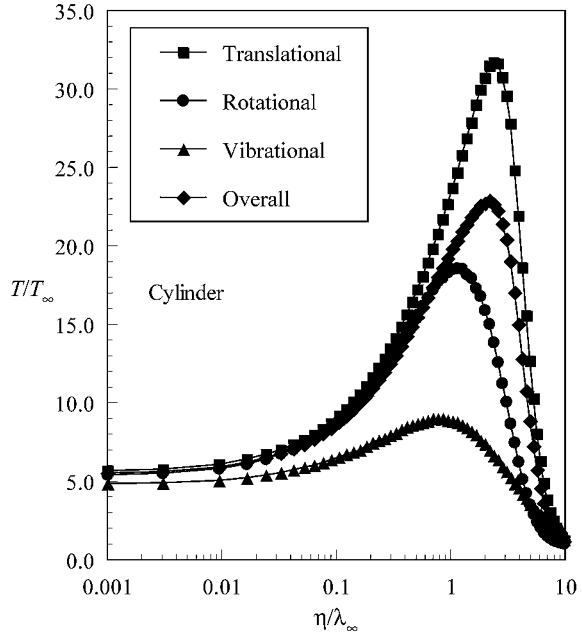

Fig. 6 Dimensionless kinetic temperature profiles along the stagnation streamline for the circular cylinder.

the flow. Insufficient upstream domain size leads to overprediction of aerodynamic heating and forces.[21] Figure 3 demonstrates that the shape of the leading edge influences the flowfield far upstream. This domain of influence increases with decreases in the power-law exponent. This influence is still stronger for the circular cylinder because it is blunter than the power-law leading edges. This behavior results from the upstream diffusion of particles that are reflected from the nose of the leading edge. Therefore, blunting the nose of the leading edge (decreasing n) leads to a significantly larger disturbance upstream of the body.

Figure 4 presents the velocity slip u_w, normalized by the freestream velocity, along the body surface as a function of the body slope angle θ (see Fig. 2). It is seen that velocity slip increases from zero at the stagnation point up to a maximum value at $\theta \approx 20$ deg, which is a function of the power-law exponent. For the $n = \frac{1}{2}$ case, the flow expands slowly, and the maximum velocity slip is 6% of the freestream velocity. For the $n = 0.8$ case, the maximum velocity slip is 12% of the freestream velocity. Hence, the outer extent of the flowfield disturbance above the surface is much smaller for a power-law exponent of 0.8 than that for $\frac{1}{2}$. Note that as the power-law exponent increases, the position of the maximum value is displaced closer to the stagnation point. As a reference, in terms of arc length along the body, the station $\theta \approx 20$ deg corresponds to $s/\lambda_\infty \approx 5.0$ and 0.7 for power-law exponents of $\frac{1}{2}$ and 0.8, respectively. Therefore, for the power-law exponent of 0.8, the maximum velocity slip takes place one order of magnitude closer to the stagnation point, as compared to the $n = \frac{1}{2}$ case.

Density profiles along the stagnation streamline for the circular cylinder and the power-law leading edges are plotted in Fig. 5. The predictions of density for the circular cylinder and all of the power law exponents investigated show no sign of a discrete shock wave. Instead, there is a continuous rise in density from the freestream to the body, rising to well above the continuum inviscid limit. As a point of reference, the Rankine–Hugoniot relations give a postshock density that corresponds to the ratio $\rho/\rho_\infty = 5.8$ for a freestream Mach number of 12. Near the stagnation point ($\eta/\lambda_\infty = 0$), a substantial density increase occurs that is a characteristic of hypersonic cold-wall flows.[21] In a typical entry flow, the body surface temperature is low compared with the stagnation temperature. The low ratio of these two temperatures leads to a steep density gradient near the body surface. For the present simulation, the ratio of wall temperature to stagnation temperature is 0.13. It can be observed from these density profiles that density rises gradually as the flow approaches the body, indicating the diffuse nature of the shock wave that is a characteristic of highly rarefied flows. For the flow conditions in the present simulation, the free molecular flow equations[15] give a density ratio of 9.89 at the stagnation point. Note that the density ratio for the $n = 0.8$ case is approaching the free-molecular value at the stagnation point. The density domain of influence upstream of the body is smaller than that for the velocity. Also, much of the density increase in the shock layer occurs after the temperature has reached its postshock value.

Figures 6–8 display the kinetic temperature profiles, normalized by the freestream temperature T_∞, for the circular cylinder and power-law exponents of $\frac{1}{2}$ and 0.8, respectively. From Figs. 6–8, thermodynamic nonequilibrium is observed throughout the shock layer, as shown by the lack of equilibrium of the translational and internal kinetic temperatures. Thermal nonequilibrium occurs when the temperatures associated with the translational, rotational, and vibrational modes of a polyatomic gas are different. The overall kinetic temperature shown is defined for a nonequilibrium gas as the weighted mean of the translational and internal temperatures.[15]

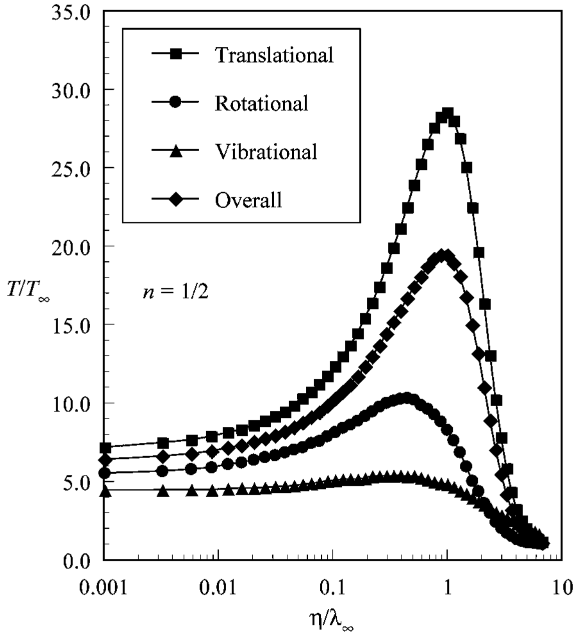

Fig. 7 Dimensionless kinetic temperature profiles along the stagnation streamline for the $n = \frac{1}{2}$ case.

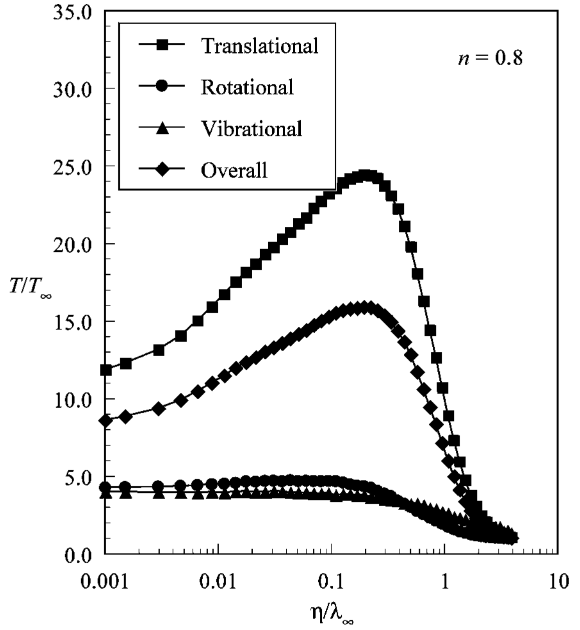

Fig. 8 Dimensionless kinetic temperature profiles along the stagnation streamline for the $n = 0.8$ case.

Note that the ideal gas equation of state does not apply to this temperature in a nonequilibrium situation. The overall kinetic temperature is equivalent to the thermodynamic temperature only under thermal equilibrium conditions.

According to Figs. 6–8, it can be seen that the temperature profiles for the power-law leading edges follow the same trend as those presented by the circular cylinder. In the undisturbed freestream far from the body, the translational and internal temperatures have the same value and are equal to the thermodynamic temperature. When the nose of the body is approached, the translational temperature rises to well above the rotational and vibrational temperatures and reaches a maximum value that is a function of the power-law exponent n. Near the nose of the body, the translational temperature decreases and reaches a value on the wall that is above the wall temperature, resulting in a temperature jump as defined in continuum formulation.[22] The temperature jump increases as the power-law exponent increases.

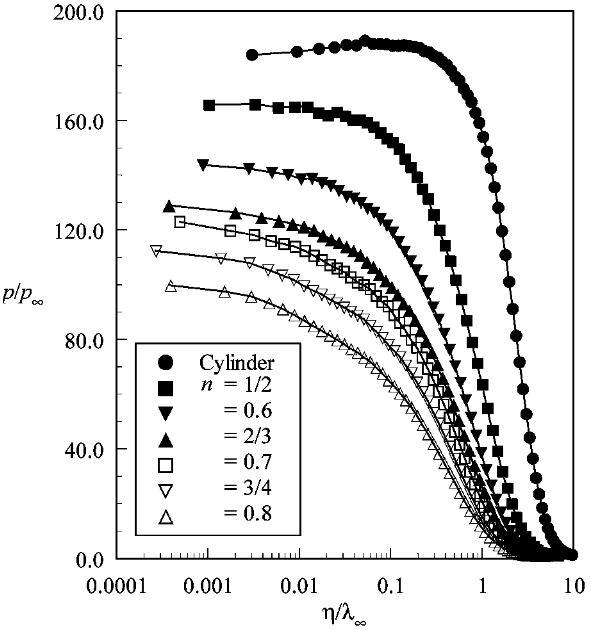

Fig. 9 Dimensionless pressure profiles along the stagnation streamline for the circular cylinder and for various power-law leading edges.

The substantial rise in translational temperature occurred before the density rise (see Fig. 5), a characteristic feature of a rarefied hypersonic shock wave.[23] For instance, the translational temperature reaches the maximum value at a distance of λ_∞ from the nose of the leading edge for a power-law exponent of $\frac{1}{2}$ (Fig. 7), whereas the density ratio has increased by only a factor of about two. The initial translational temperature rise results from the essentially bimodal velocity distribution, the molecular sample consisting of mostly undisturbed freestream molecules along with the molecules that have been affected by the shock and reflected from the body. In this way, the translational temperature rise is a consequence of the large velocity separation between these two classes of molecules. The bimodal velocity distribution was pointed out by Liepmann et al.[24] The difference between translational temperature and the internal temperature at the stagnation point also indicates that thermodynamic equilibrium is not achieved in the boundary layer. The difference between the temperature components in the shock layer decreases at a lower power-law exponent n because the collision rate increases due to the higher density (see Fig. 5). The vibrational temperature increases much more slowly as the power-law exponent increases. As this process is density dependent, the difference between the translational temperature and vibrational temperature increases as the power-law exponent increases.

Pressure profiles along the stagnation line are shown in Fig. 9 for the circular cylinder and for the power-law shapes. In Fig. 9, pressure is normalized by the freestream pressure p_∞. As can be seen, there is a continuous rise in pressure from the freestream up to the nose of the power-law leading edges. Near the stagnation point, a substantial pressure increase occurs. This pressure increase is a function of the power-law exponent n. Greater n corresponds to a lower pressure value at the stagnation point. Also, note that, as the power-law exponent decreases, the pressure tends to a constant value close to the stagnation point. The extent of the upstream flowfield disturbance for pressure is significantly different from those presented by density and temperature. The domain of influence for pressure is higher than that for density and lower than that presented for temperature. Similar to the density, much of the pressure increase in the shock layer occurs after the translational temperature has reached its postshock value.

Surface Quantities

The pressure p_w on the body is calculated by averaging the normal momentum transfer of the molecules impinging on the surface. Results are presented in terms of the dimensionless pressure coefficient c_p and the dimensionless distance s/λ_∞ along the surface,

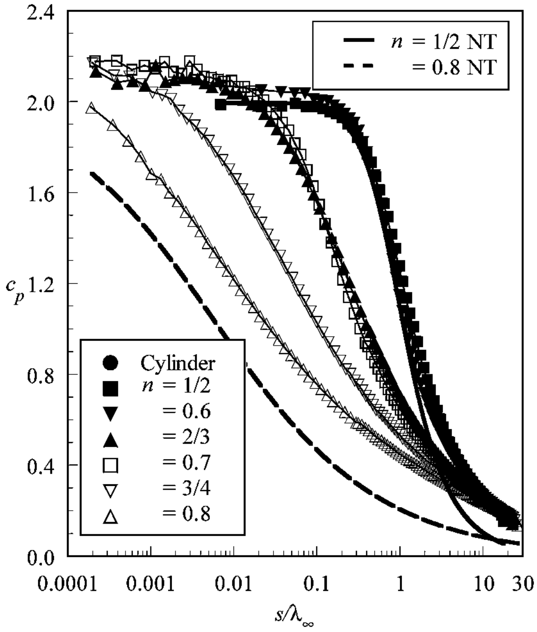

Fig. 10 Pressure coefficient as a function of the arc length for the circular cylinder and for various power-law leading edges.

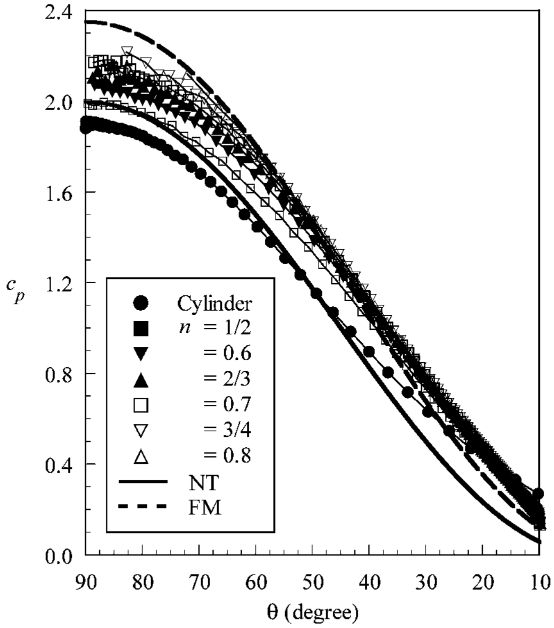

Fig. 11 Pressure coefficient as a function of the body slope angle for the circular cylinder and for various power-law leading edges.

measured from the stagnation point. The effect of the power-law exponent on the pressure coefficient obtained with a DSMC method is illustrated in Fig. 10 for power-law exponents of $\frac{1}{2}$, 0.6, $\frac{2}{3}$, 0.7, $\frac{3}{4}$, and 0.8. For comparison purposes, Fig. 10 also illustrates the pressure coefficient for the circular cylinder case and the pressure coefficient predicted by Newtonian theory for power-law exponents of $\frac{1}{2}$ and 0.8. Symbols correspond to the DSMC results, and lines to the Newtonian results. For the $n = \frac{1}{2}$ case, the pressure coefficient obtained by DSMC simulations agrees with that by Newtonian theory in the vicinity of the nose, that is, by a distance around a freestream mean free path λ_∞. For the other case shown, the $n = 0.8$ case, the pressure coefficient obtained by the Newtonian theory is lower than that obtained by the DSMC simulations along the arc length investigated. Typically, the Newtonian flow theory underpredicts the pressure on two-dimensional thin body flowfields.

Another important feature of the pressure coefficient is related to the pressure coefficient gradient $\mathrm{d}c_p/\mathrm{d}s$ along the arc length as the arc length goes to zero. According to Mason and Lee,[11] by the use of Newtonian theory, the pressure coefficient gradient $\mathrm{d}c_p/\mathrm{d}s$ goes to zero for $n < \frac{2}{3}$, a characteristic of a blunt body. The pressure coefficient gradient is finite for $n = \frac{2}{3}$ and goes to minus infinite for $n > \frac{2}{3}$, a characteristic of a sharp body. In this way, there is a region, defined by $\frac{1}{2} < n < \frac{2}{3}$, where the pressure gradient behaves as if the body were a blunt one, in spite of the leading edge having a zero radius of curvature. The pressure gradient might be obtained from the curves presented in Fig. 10 by a curve-fitting process. However, the derivative of the solution yielded by the curve fitting may result in a wrong conclusion. To avoid this possible error, a different procedure has been adopted here. The pressure coefficient gradient along the arc length may be obtained by

$$\frac{\mathrm{d}c_p}{\mathrm{d}s} = \frac{\mathrm{d}c_p}{\mathrm{d}\theta} \cdot \frac{\mathrm{d}\theta}{\mathrm{d}s} = \frac{\mathrm{d}c_p/\mathrm{d}\theta}{\mathrm{d}s/\mathrm{d}\theta} \tag{2}$$

By the use of the definition of the arc length, the definition of the body slope, along with Eq. (1), $\mathrm{d}s/\mathrm{d}\theta$ results in the following equation:

$$\frac{\mathrm{d}s}{\mathrm{d}\theta} = -\frac{(an)^{1/(1-n)}}{(1-n)} \frac{(\cos\theta)^{(2n-1)/(1-n)}}{(\sin\theta)^{(2-n)/(1-n)}} \tag{3}$$

The pressure coefficient shown in Fig. 10 as a function of the dimensionless arc length s/λ_∞ is presented in Fig. 11 as a function of the body slope angle θ, which changes from 90 deg at the nose of the leading edge to 10 deg at the tangency point (see Fig. 1). Plotted along with the DSMC solutions are the pressure coefficients predicted by the Newtonian theory and by the free-molecular flow. Plotted in this way, the pressure coefficients predicted by both Newtonian theory and free-molecular flow are independent of the power-law exponent, and they represent any geometry where the body slope angle changes from 90 deg at the nose to 10 deg downstream of the nose. Also, note that the DSMC solutions are between these two limits in the vicinity of the nose. As the power-law exponent increases, the pressure coefficient approaches that predicted by the free-molecular flow. Furthermore, these two limits are obtained by an explicit relation for c_p. Consequently, explicit relations for $\mathrm{d}c_p/\mathrm{d}\theta$ are obtained to investigate $\mathrm{d}c_p/\mathrm{d}s$ in Eq. (2). The pressure coefficient on the body surface given by the free-molecular flow analysis[15] is as follows:

$$c_p = \left(1/S_\infty^2\right)\left\{\left[z/\sqrt{\pi} + \tfrac{1}{2}(T_w/T_\infty)^{\frac{1}{2}}\right]\exp(-z^2) + \left[\tfrac{1}{2} + z^2 + \tfrac{1}{2}(T_w/T_\infty)^{\frac{1}{2}}\sqrt{\pi}z\right][1 + \operatorname{erf}(z)] - 1\right\} \tag{4}$$

where $z = S_\infty \sin\theta$ and $S_\infty = U_\infty/\sqrt{(2RT_\infty)}$ is the molecular speed ratio.

As a result, $\mathrm{d}c_p/\mathrm{d}\theta$ is given by the following equation:

$$\frac{\mathrm{d}c_p}{\mathrm{d}\theta} = \frac{1}{S_\infty}\left\{\frac{2}{\sqrt{\pi}}\exp(-z^2) + \left[2z + \frac{\sqrt{\pi}}{2}\left(\frac{T_w}{T_\infty}\right)^{\frac{1}{2}}\right][1 + \operatorname{erf}(z)]\right\}\cos\theta = C(\theta)\cos\theta \tag{5}$$

where $C(\theta)$ represents all of the terms inside the brackets divided by S_∞.

By the substitution of Eqs. (3) and (5) into Eq. (2), $\mathrm{d}c_p/\mathrm{d}s$ is found:

$$\frac{\mathrm{d}c_p}{\mathrm{d}s} = -\frac{(1-n)}{(an)^{1/(1-n)}} \cdot C(\theta) \cdot (\sin\theta)^{(2-n)/(1-n)} \cdot (\cos\theta)^{(2-3n)/(1-n)} \tag{6}$$

When the limit as $\theta \to 90$ deg is investigated, it is seen that $C(\theta)$ and $\sin\theta$ are positive and finite for $0 < n < 1$. Therefore, the exponent in the cosine term will dictate the behavior of the pressure gradient. In this way, it is found that the pressure gradient at the nose of the leading edge goes to zero for $n < \frac{2}{3}$, it is finite for $n = \frac{2}{3}$, and it goes to minus infinite for $n > \frac{2}{3}$. This result is exactly the same as that predicted by the Newtonian theory. Note that $\mathrm{d}c_p/\mathrm{d}\theta$ for

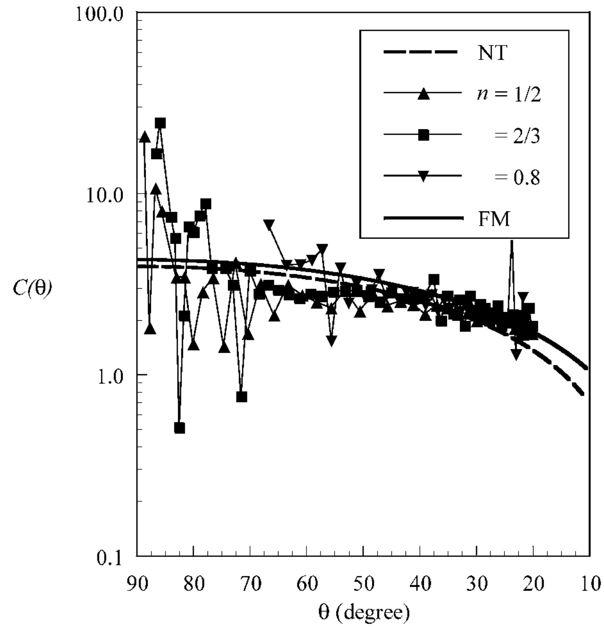

Fig. 12 Function $C(\theta)$ as a function of the body slope angle for power-law exponents of $\frac{1}{2}$, $\frac{2}{3}$, and 0.8.

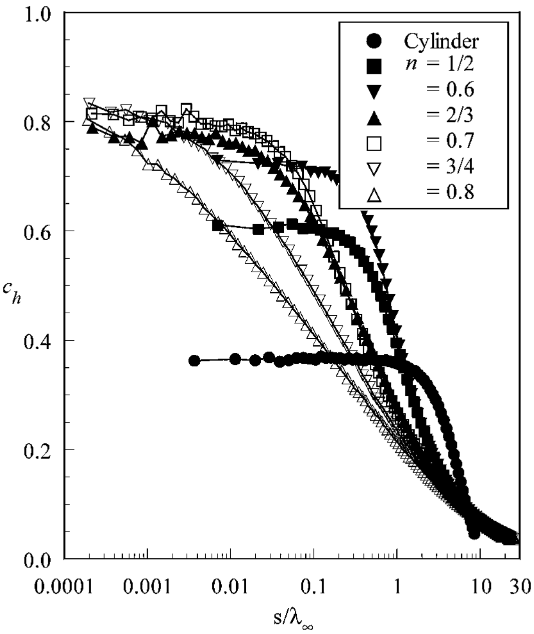

Fig. 13 Heat transfer coefficient as a function of the arc length for the circular cylinder and for various power-law leading edges.

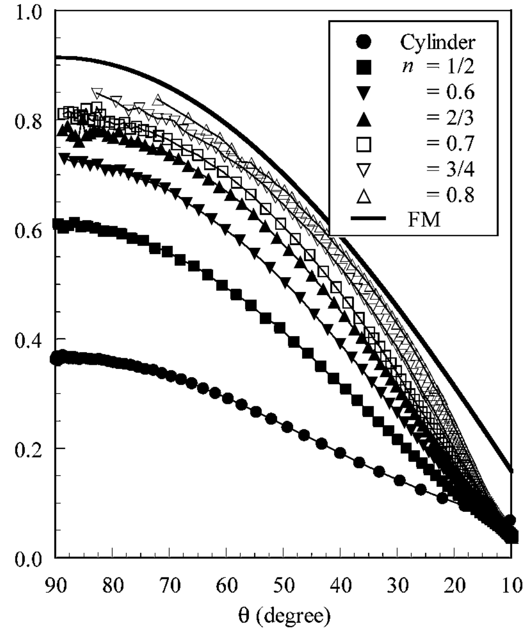

Fig. 14 Heat transfer coefficient as a function of the body slope angle for the circular cylinder and for various power-law leading edges.

Newtonian theory is given by $4\sin\theta\cos\theta$, or, in a simplified form, by $C(\theta)\cos\theta$. This simplified form is similar to the term in the right-hand side of Eq. (5), where the trigonometric term is $\cos\theta$. In conclusion, if the pressure gradients for the two limits shown in Fig. 11 (i.e., for Newtonian theory and free-molecular flow) follow the same behavior, then it is expected that the pressure gradients from the DSMC results behave in the same manner. In this way, $\mathrm{d}c_p/\mathrm{d}\theta$ might follow the same form as $C(\theta)\cos\theta$, where $C(\theta)$ stands for a generic function. To investigate this behavior further, $\mathrm{d}c_p/\mathrm{d}\theta$ for each leading-edge shape is estimated by assuming the following equation:

$$\frac{\mathrm{d}c_p}{\mathrm{d}\theta} \approx \frac{\Delta c_p}{\Delta\theta} = \left(\frac{\Delta c_p}{\cos\theta\,\Delta\theta}\right)\cos\theta = C(\theta)\cos\theta \qquad (7)$$

Hence, if the function $C(\theta)$ for DSMC results, defined by the term inside the bracket, presents the same trend as those for Newtonian theory and free-molecular flow, then $\mathrm{d}c_p/\mathrm{d}s$ will be given by Eq. (7). Figure 12 presents a comparison of the function $C(\theta)$ for the computational results, the Newtonian theory, and free-molecular flow. Although the computational results present fluctuations as the body slope angle θ approaches the nose of the leading edge, it is seen that the curves for $C(\theta)$ clearly suggest that $\mathrm{d}c_p/\mathrm{d}\theta$ for the computational results follows the function $C(\theta)\cos\theta$ as assumed in Eq. (7). Consequently, these results appear to show that pressure coefficient gradient $\mathrm{d}c_p/\mathrm{d}s$ for the computational results presents the same trend as those predicted by the Newtonian theory and free-molecular flow. Hence, the pressure coefficient goes to zero for $n < \frac{2}{3}$, it is finite for $n = \frac{2}{3}$, and it goes to minus infinite for $n > \frac{2}{3}$, as the body slope angle goes to 90 deg or the arc length goes to zero. This is an indication that there is a class of power-law shapes, $n > \frac{2}{3}$, that produces a flowfield that does not exhibit classical blunt-body behavior and can be considered sharp for the calculation of the pressure distribution.

The heat flux q_w to the body is calculated by averaging the energy of the molecules impinging on the surface. The heat flux was normalized by $\frac{1}{2}\rho_\infty U_\infty^3$, which corresponds to 2 MW/m^2 for the freestream conditions, and which is presented in terms of dimensionless heat transfer coefficient c_h. The heat transfer coefficient c_h was based on the gas–surface interaction model of fully accommodated, completely diffuse reemission. This is the most common model assumed, even though it is well known that some degree of specular reemission and less than complete accommodation are more realistic assumptions. Furthermore, care should be taken in choosing the thermal accommodation coefficient for different altitude ranges, because the value of a thermal accommodation coefficient has a significant impact on the predicted aerodynamic heating, as pointed out by Gilmore and Harvey.[25]

The heat transfer coefficient c_h is illustrated in Fig. 13 as a function of the dimensionless distance s/λ_∞ along the surface measured from the stagnation point. The leading-edge geometry effect is demonstrated by comparing the computational results for the circular cylinder and for the power-law shapes. Note that the heat transfer coefficient is sensitive to the power-law exponent n near the stagnation point. The maximum value occurs at the stagnation point and drops off sharply a short distance away from the leading edge as the power-law exponent increases. The leading-edge geometry effect can also be seen by comparing the computational results with these predicted by free-molecular flow. Figure 14 presents this comparison for the heat transfer coefficient as a function of the body slope angle θ. These curves indicate that the heat transfer coefficient increases as the leading edge becomes aerodynamically sharp and approaches the free-molecular value for the conditions investigated in this work, a behavior observed earlier in the other properties.

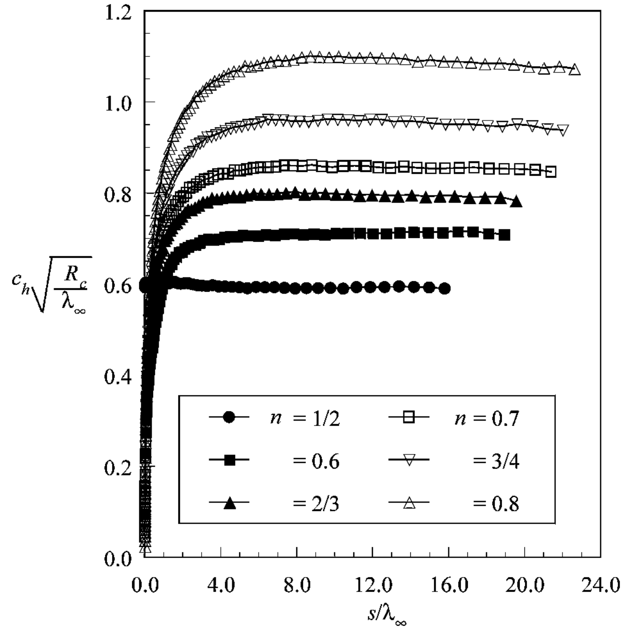

Fig. 15 Heat transfer coefficient as a function of the arc length for various power-law leading edges.

According to the literature,[26] theoretical formulations, experimental data, and semi-empirical formulas all agree that the heat flux at the stagnation point of a blunt body varies inversely with the square root of the nose radius. To verify this dependence, the product $c_h\sqrt{(R_c/\lambda_\infty)}$ is obtained from the DSMC results for the power-law shapes investigated, where R_c is the local radius of curvature. Figure 15 presents this product as a function of the dimensionless arc length along the body surface. As would be expected, the dependence of the heat transfer coefficient on the radius of curvature in the stagnation region does not hold for power-law leading edges defined by $n > \frac{1}{2}$. However, for the only case of finite radius of curvature at the stagnation point, the $n = \frac{1}{2}$ case, the heat flux to the body follows the qualitative behavior predicted by the continuum theory for a classical blunt body. Furthermore, it is seen that the heat flux to the body is inversely proportional to the square root of the curvature radius of the power-law shapes far from the stagnation region, independently of the power-law exponent.

The skin friction τ_w on the body is calculated by averaging the parallel momentum transfer of the molecules impinging on the surface. Results are normalized by $\frac{1}{2}\rho_\infty U_\infty^2$ and presented in terms of the dimensionless skin-friction coefficient c_f and the dimensionless distance s/λ_∞ along the surface measured from the stagnation point. The leading-edge geometry effect on the skin-friction coefficient is illustrated in Fig. 16 for various power-law exponents and for the circular cylinder. Along the surface, the value of c_f starts from zero at the stagnation point, increases to a maximum value near the leading edge, and decreases downstream along the body surface. A larger n leads to a higher peak value for the skin-friction coefficient. Also, a larger n displaces the peak value close to the stagnation point. The skin-friction coefficient presents interesting features as it is plotted as a function of the body slope angle θ. Figure 17 shows these features, as well as a comparison with the skin-friction coefficient, by assuming free-molecular flow. Note that the skin-friction coefficient predicted by free molecular-flow exhibits the maximum value at 45 deg. Similarly, the maximum values for the power-law leading edges occur very close to the same station, that is, 45 deg. Attention should be paid to the 45-deg station corresponding to a completely different arc length s/λ_∞ as the power-law exponent increases from $\frac{1}{2}$ to 0.8. As a point of reference, the slope angle of 45 deg for a circular cylinder and power-law exponents of $\frac{1}{2}$ and 0.8 corresponds to $s/\lambda_\infty \approx 4.0$, 1.0, and 0.007, respectively. Thus, for a power-law exponent of 0.8, the peak value for the skin friction occurs in a location almost three orders of magnitude closer to the stagnation point than that for either the power-law exponent of $\frac{1}{2}$ or for the circular cylinder.

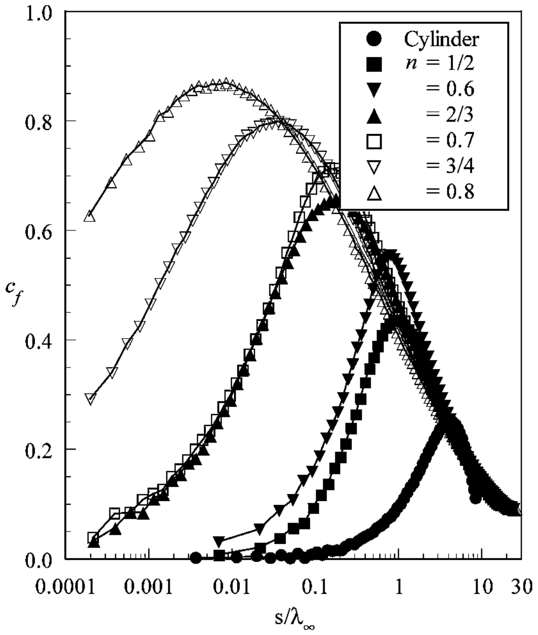

Fig. 16 Skin-friction coefficient as a function of the arc length for the circular cylinder and for various power-law leading edges.

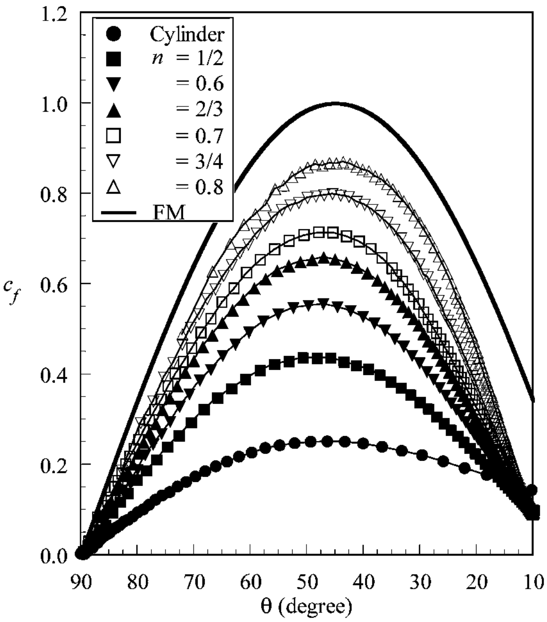

Fig. 17 Skin-friction coefficient as a function of the body slope angle for the circular cylinder and for various power-law leading edges.

The total drag coefficient c_d was obtained by the integration of the pressure and shear stress distributions from the nose of the leading edge to the station L (see Fig. 1), which corresponds to the tangent point common to all of the body shapes. The total drag is divided into its components of pressure drag and skin-friction drag. Note that the values for the total drag presented in this section were obtained by assuming that the shapes acted as leading edges. Therefore, no base pressure effects were taken into account on the calculations. Figure 18 illustrates the total drag coefficient, normalized by $\frac{1}{2}\rho_\infty U_\infty^2 H$, as a function of the power-law exponent n. As $n \to \frac{1}{2}$, the pressure drag contribution to the total drag coefficient is larger than that presented by the skin-friction drag, a characteristic of a blunt body. However, as $n \to 0.8$, the total drag coefficient is dominated by the skin-friction drag, a characteristic of a sharp body. Because the net effect on total drag depends on these opposite behaviors, appreciable changes are observed in the total drag coefficient for the power-law exponent range investigated. As a reference, the drag coefficient for the $n = \frac{1}{2}$ case is around 17% higher than that for the $n = 0.8$ case. For the circular cylinder case (not shown),

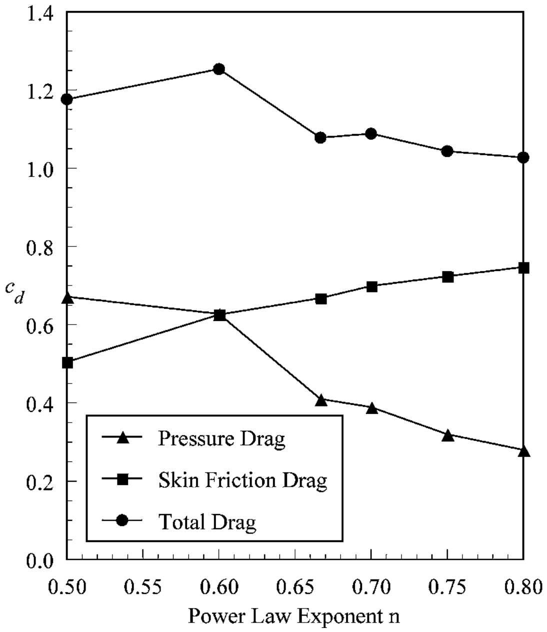

Fig. 18 Pressure drag, skin-friction drag, and total drag coefficients as a function of the power-law exponent.

the pressure drag, the skin-friction drag, and the total drag coefficient are 1.333, 0.169, and 1.502, respectively. Thus, compared to the power-law shapes, the circular cylinder presents a high value for the total drag coefficient, where the major contribution is given by the pressure drag coefficient.

Conclusions

Through the use of DSMC method, the flow structure and the surface quantities about power-law shapes have been investigated. The calculations provided information concerning the nature of the flow at the vicinity of the nose resulting from variations in the body shape for the idealized situation of two-dimensional hypersonic rarefied flow. Performance results for power-law exponents of $\frac{1}{2}$, 0.6, $\frac{2}{3}$, 0.7, $\frac{3}{4}$, and 0.8 were compared to that of the corresponding circular cylinder that defined their geometries. Very detailed descriptions of the flow properties, such as velocity, density, temperature, and pressure, were presented separately in the stagnation region of the power-law shaped leading edges by a numerical method that properly accounts for nonequilibrium effects.

It was observed that the shape of the leading edge disturbed the flowfield far upstream, as compared to the freestream mean free path, and the domain of influence decreased as the leading edge became aerodynamically sharp. The simulations confirmed the qualitative behavior of the pressure gradient predicted by the Newtonian theory. It was found that the pressure gradient along the body surface goes to zero at the nose of the leading edge for $n < \frac{2}{3}$; it is finite for $n = \frac{2}{3}$ and goes to minus infinite for $n > \frac{2}{3}$. Thus, there is a class of power-law shapes, $n > \frac{2}{3}$, that produces a flowfield that does not exhibit classical blunt-body behavior, and the shapes can be considered sharp for the calculation of the pressure distribution. In this context, shapes given by $\frac{1}{2} < n \leq \frac{2}{3}$ correspond to geometrically and aerodynamically blunt bodies. Nevertheless, for $\frac{2}{3} < n < 1$, the shapes correspond to geometrically blunt and aerodynamically sharp bodies. Finally, it was found that the stagnation point heating for power-law leading edges with a finite radius of curvature followed the relation predicted by the continuum theory. For those power-law leading edges with zero radii of curvature, the stagnation point heating is not a function of the radius of curvature in the vicinity of the nose but agrees with the continuum prediction far from the stagnation point for the leading edges investigated.

Acknowledgments

This research was supported by the Conselho Nacional de Desenvolvimento Científico e Tecnológico from Brazil (CNPq Grant 200368/88.5). The authors are grateful to the High Performance Computer Center at the Universidade Federal do Rio de Janeiro (Federal University of Rio de Janeiro) and Centro de Previsão de Tempo e Estudos Climáticos (The Weather Prediction Center and Climate Studies) for use of the workstations.

References

[1] Yasuhara, M., "On the Hypersonic Viscous Flow past Slender Bodies of Revolution," *Journal of the Physical Society of Japan*, Vol. 11, No. 8, 1956, pp. 878–886.

[2] Lees, L., and Kubota, T., "Inviscid Hypersonic Flow over Blunt-Nosed Slender Bodies," *Journal of the Aeronautical Sciences*, Vol. 24, No. 3, 1957, pp. 195–202.

[3] Mirels, H., "Hypersonic Flow over Slender Bodies Associated with Power-Law Shocks," *Advances in Applied Mechanics*, Vol. 7, 1962, pp. 1–54.

[4] Freeman, N. C., Cash, R. F., and Bedder, D., "An Experimental Investigation of Asymptotic Hypersonic Flows," *Journal of Fluid Mechanics*, Vol. 18, No. 3, 1964, pp. 379–384.

[5] Beavers, G. S., "Shock-Wave Shapes on Hypersonic Axisymmetric Power-Law Bodies," *AIAA Journal*, Vol. 7, No. 10, 1969, pp. 2038–2040.

[6] Guiraud, J. P., Vallée, D., and Zolver, R., "Bluntness Effects in Hypersonic Small Disturbances Theory," *Basic Development in Fluid Dynamics*, edited by M. Holt, Vol. 1, 1st ed., Academic Press, New York, 1965, pp. 127–247.

[7] Townsend, J. C., "Hypersonic Aerodynamic Characteristics of a Family of Power-Law, Wing–Body Configurations," NASA TN D-7427, Dec. 1973.

[8] Townsend, J. C., "Second-Order Small-Disturbance Solutions for Hypersonic Flow over Power-Law Bodies," NASA TN D-7973, Nov. 1975.

[9] Merlen, A., and Andriamanalina, D., "Analytical Solutions for Hypersonic Flow past Slender Power-Law Bodies at Small Angle of Attack," *AIAA Journal*, Vol. 30, No. 11, 1992, pp. 2683–2693.

[10] Mason, W. H., and Lee, J., "Minimum-Drag Axisymmetric Bodies in the Supersonic/Hypersonic Flow Regimes," *Journal of Spacecraft and Rockets*, Vol. 31, No. 3, 1994, pp. 406–413.

[11] Mason, W. H., and Lee, J., "Aerodynamically Blunt and Sharp Bodies," *Journal of Spacecraft and Rockets*, Vol. 31, No. 3, 1994, pp. 378–382.

[12] Merlen, A., Fabre, E., and Cieslak, S., "Analytical Hypersonic Waverider Configurations," *Proceedings of the 20th International Symposium on Shock Waves*, Vol. 1, edited by B. Sturtevant, J. E. Shepherd, and H. G. Hornung, 1995, pp. 299–304.

[13] O'Brien, T. F., and Lewis, M. J., "Power-Law Shapes for Leading-Edge Blunting with Minimal Shock Standoff," *Journal of Spacecraft and Rockets*, Vol. 36, No. 5, 1999, pp. 653–658.

[14] Van Dyke, M. D., "A Study of Hypersonic Small-Disturbance Theory," NACA TN 3173, 1954.

[15] Bird, G. A., *Molecular Gas Dynamics and the Direct Simulation of Gas Flows*, 1st ed., Oxford Univ. Press, Oxford, 1994.

[16] Bird, G. A., "Monte Carlo Simulation in an Engineering Context, *Rarefied Gas Dynamics*, Pt. 1, edited by Sam S. Fisher, Vol. 74, Progress in Astronautics and Aeronautics, AIAA, New York, 1981, pp. 239–255.

[17] Borgnakke, C., and Larsen, P. S., "Statistical Collision Model for Monte Carlo Simulation of Polyatomic Gas Mixture," *Journal of Computational Physics*, Vol. 18, No. 4, 1975, pp. 405–420.

[18] Bird, G. A., "Definition of Mean Free Path for Real Gases," *Physics of Fluids*, Vol. 26, No. 11, 1983, pp. 3222, 3223.

[19] Santos, W. F. N., "Direct Simulation Monte Carlo of Rarefied Hypersonic Flow on Power Law Shaped Leading Edges," Ph.D. Dissertation, Dept. of Aerospace Engineering, Univ. of Maryland, College Park, MD, Dec. 2001.

[20] Bertin, J. J., *Hypersonic Aerothermodynamics*, 1st ed., AIAA Education Series, AIAA, Washington, DC, 1994, pp. 22–25.

[21] Haas, B. L., and Fallavollita, M. A., "Flow Resolution and Domain Influence in Rarefied Hypersonic Blunt-Body Flows," *Journal of Thermophysics and Heat Transfer*, Vol. 8, No. 4, 1994, pp. 751–757.

[22] Gupta, R. N., Scott, C. D., and Moss, J. N., "Slip-Boundary Equations for Multicomponent Nonequilibrium Airflow," NASA TP-2452, Nov. 1985.

[23] Bird, G. A., "Thermal and Pressure Diffusion Effects in High Altitude Flows," AIAA Paper 88-2732, June 1988.

[24] Liepmann, H. W., Narasimha, R., and Chahine, M., "Theoretical and Experimental Aspects of the Shock Structure Problem," *Proceedings of the 11th International Congress of Applied Mechanics*, edited by H. Gortler, 1964, pp. 973–979.

[25] Gilmore, M. R., and Harvey, J. H., "Effects of Mach Number, T_{wall}, T_{∞}, and Thermal Accommodation Coefficient on Flow Around Bluff Bodies in Rarefied Regime," *Rarefied Gas Dynamics: Space Science and Engineering*, edited by B. D. Shizgal and D. P. Weaver, Vol. 160, Progress in Astronautics and Aeronautics, AIAA, Washington, DC, 1994, pp. 308–322.

[26] Anderson, J. D., Jr., *Hypersonic and High Temperature Gas Dynamics*, 1st ed., McGraw–Hill, New York, 1989, p. 256.

I. D. Boyd
Associate Editor